

# Measurement of Tendon Strain During Muscle Twitch Contractions Using Ultrasound Elastography

Joe Farron, Tomy Varghese, and Darryl G. Thelen

**Abstract**—A 2-D strain estimation algorithm was used to estimate tendon strain from ultrasound data collected during muscle twitch contractions. We first used speckle tracking techniques to estimate frame-to-frame displacements of all pixels within a rectangular region of interest (ROI) positioned over a tendon. A weighted, least-squares approach was then solved for the displacements of the ROI endpoints that best fit the pixel displacements. We summed endpoint displacements across successive frames to determine the cumulative endpoint motion, which was then used to estimate the cumulative strain along the tendinous fibers. The algorithm was applied to ultrasound radiofrequency data, acquired at 74 frames per second over the tibialis anterior (TA) musculotendon junction (MTJ). The TA muscle was electrically stimulated with the subject holding voluntary preloads of 0%, 10%, 20%, 30%, 40%, and 50% of a maximum voluntary contraction (MVC). Peak tendon strains computed using elastography (0.06 to 0.80%) were slightly larger and occurred earlier (50–90 ms after stimulus) than calculations based on visual analysis of B-mode images. This difference likely reflected the more localized nature of the elastographic strain values. Estimates of the tangential elastic modulus ( $192 \pm 58$  MPa) were consistent with literature values obtained using more direct approaches. It is concluded that automated elastographic approaches for computing in vivo tendon strains could provide new insights into musculotendon dynamics and function.

## I. INTRODUCTION

ULTRASOUND is increasingly being used to characterize in vivo musculotendon mechanics. A common approach is to use visual inspection of B-mode images to identify anatomical landmarks, e.g., the musculotendon junction (MTJ), with the muscle in relaxed and contracted states. The relative motion between frames has been used to estimate various biomechanical quantities such as the average strain in the tendon [1]–[3], muscle fiber pennation angles [4], and moment arms about a joint [5]. Strain estimates have also been coupled with measurements of external force produced by muscle contractions to obtain estimates of the tissue stress and stiffness [6], [7]. These

studies have provided novel insights into musculotendon interactions under both static loading and dynamic conditions such as walking [8], [9]. However, the manual digitization of anatomical landmarks is time-consuming and does not provide high spatial resolution, thereby limiting the information that can be obtained.

The development of automated elastographic approaches for tracking musculotendon displacements could both expand the use of ultrasound in biomechanics and improve the resolution of strain measurements. A primary challenge is that current elastographic techniques best track motion along the beam axis [10], and it is extremely difficult to align an ultrasound transducer beam in the muscle and tendinous fiber directions. Although 2-D tracking algorithms have been introduced in recent years [11]–[13], the lateral displacement estimates generally do not exhibit the resolution achieved in the axial direction. Prior studies that have used elastographic approaches to track muscle tissue have either only analyzed the axial strains [14] or relied on B-mode images [15], which cannot provide the same high spatial resolution as radiofrequency (RF) data [10].

The purpose of this study was to develop and evaluate the use of an RF elastography algorithm for estimating the strain along tendinous fibers during a muscular twitch contraction. Our experiments were performed on the tibialis anterior, a superficial dorsiflexor of the ankle, undergoing twitch contractions. Strain estimates were compared with the timing and magnitude of strains determined from visual analysis of B-mode images. We also recorded the external force induced by the twitch, providing a basis for estimating the stress and tangential modulus of the tendinous tissue.

## II. METHODS

### A. Data Acquisition

Five subjects (2 females, 3 males, age  $27.4 \pm 4.6$  years, height  $179 \pm 7$  cm, body mass  $73 \pm 9$  kg) with no recent lower limb injury participated in this study. Each subject was seated with right hip, knee and ankle angles of 90, 45, and 0 degrees, respectively. Subjects wore a stiff-soled bicycle shoe that was attached to a fixed load cell (LC101–200, Omegadyne, Stamford, CT) near the metatarsal joint (Fig. 1). Force data from the load cell was recorded at 1000 Hz using Labview software (National Instruments,

Manuscript received August 13, 2007; accepted July 20, 2008. We gratefully acknowledge the support provided by the Aircast Foundation and NIH Grant Number R01 AR56201.

J. Farron and D. G. Thelen are with the Department of Mechanical Engineering, University of Wisconsin-Madison, Madison, WI (e-mail: thelen@engr.wisc.edu).

T. Varghese and D. G. Thelen are with the Department of Biomedical Engineering, University of Wisconsin-Madison, Madison, WI.

T. Varghese is also with the Department of Medical Physics, University of Wisconsin-Madison, Madison, WI.

Digital Object Identifier 10.1109/TUFFC.2009.1002

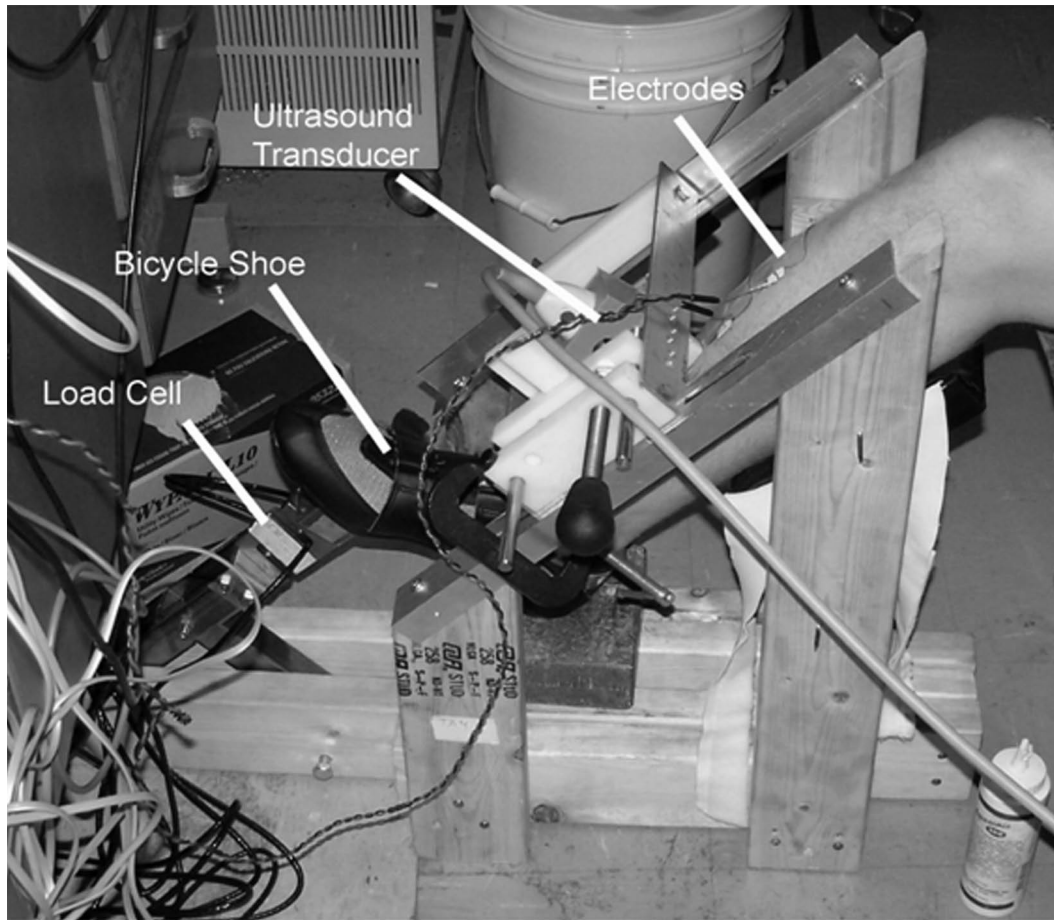


Fig. 1. Subjects were seated with their right shoe rigidly attached to a fixed load cell. An external fixture was used to position the ultrasound transducer over the musculotendon junction of the tibialis anterior muscle. Surface stimulation electrodes were used to induce muscle twitch contractions.

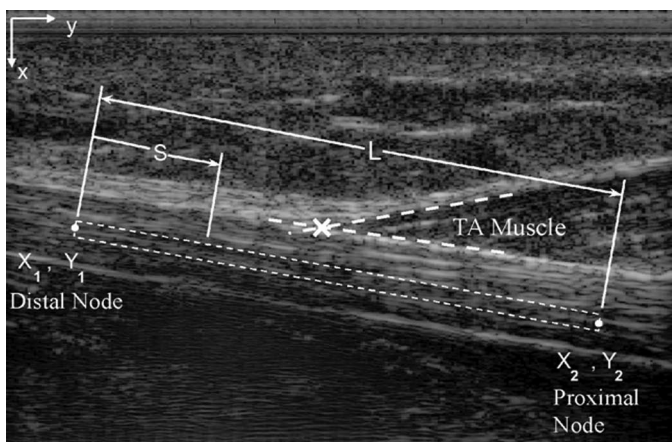


Fig. 2. The region of interest (ROI) was defined as a rectangular region of width 0.75 mm extending between distal  $(X_1, Y_1)$  and proximal  $(X_2, Y_2)$  nodes along the tendon. The length  $L$  of the ROI was tracked by computing the displacements of all pixels within the ROI and then assuming that displacements varied linearly with the distance  $S$  from the distal node. Visual inspection was used to estimate the location of the musculotendon junction (MTJ) in each B-mode image, which was defined as the intersection of straight lines along the upper TA muscle and tendon boundaries (marked by X on image).

Austin, TX). The perpendicular distance between the load cell, ankle, and heel support was measured and subsequently used with force measurements to compute the ankle joint moment.

Ultrasound images of the distal tibialis anterior (TA) musculotendon junction (MTJ) were recorded using a Siemens Antares SONOLINE (Siemens Medical Solutions Inc., Mountain View, CA) clinical ultrasound scanner. A custom fixture was used to position a VFX 13-5 transducer over the TA such that the MTJ was in the middle third of the image when the muscle was relaxed (Fig. 2). Radio-frequency (RF) data (centered at 11 MHz) were acquired over a 2 cm deep by 4 cm wide window (1036 samples/line by 244 A-lines) at a rate of 74 frames per second. The RF data were subsequently upsampled by a factor of 4 by linear interpolation in both the axial and lateral directions to increase the spatial sampling density of the computed correlation functions. The effects of upsampling the data was analyzed using synthetically generated RF data (see appendix).

Initially, the subject was asked to perform a maximum voluntary contraction (MVC), during which the maximum load cell force was recorded. Surface electrodes (51 × 51 mm square electrodes, ConMed Corporation, Utica, NY)

$$\rho_{nm}(k,l) = \frac{\sum_{i=-K}^K \sum_{j=-L}^L [F_1(n+i, m+j)F_2(n+k+i, m+l+j)]}{\left[ \sum_{i=-K}^K \sum_{j=-L}^L [F_1(n+i, m+j)]^2 \right]^{1/2} \left[ \sum_{i=-K}^K \sum_{j=-L}^L [F_2(n+k+i, m+l+j)]^2 \right]^{1/2}} \quad (1)$$

were then applied to the skin over the mid-belly of the tibialis anterior muscle for inducing twitch contractions (Fig. 1). A dual-channel, current-controlled stimulator (Grass S88, Astro-Med, Inc., West Warwick, RI) was used to initiate twitch contractions using a single current-controlled pulse (300  $\mu$ s, 50 mA). Subjects were asked to hold target force levels of 0, 10, 20, 30, 40, and 50% of MVC before the stimulation pulse being introduced, with the desired and actual force level displayed to the subject graphically on a computer monitor. Three trials at each target force level were performed in a randomized order.

Following the trials, the location of the ultrasound transducer was marked on the skin surface at the distal and proximal ends of the transducer. The cross section of the tendon was imaged at these marked locations by orienting the transducer perpendicular to the fiber direction. These B-mode images were subsequently used to measure the cross-sectional area of the tendinous tissue by tracing the tissue boundary. The skin markings were also used to measure the distal TA tendon length in a relaxed state. To do this, the insertion of the tendon was palpated in the subject's foot, and the distance from each mark to the insertion was measured using a flexible measuring tape. In post-processing each image, the MTJ was found relative to the distal end of the ultrasound images, and this distance was added to the relaxed tendon length to estimate the tendon length from the MTJ to the insertion on the foot.

### B. Elastography-Based Analysis of Tendon Strain

Calculation of cumulative displacements and strain along the tendon fiber direction involved the following steps:

- 1) A region of interest (ROI) along the direction of the tendinous fibers was defined in the first frame of data by the researcher.
- 2) Frame-to-frame displacements of 2 nodes at the distal and proximal ends of the ROI were computed.
- 3) The nodal displacements were summed and used to compute the net change in length along the ROI and, correspondingly the cumulative strain along the tendinous tissue.

Following is a detailed description of this process.

1) *Defining the ROI:* For each trial, a line segment was first established in an initial B-mode image by selecting

2 endpoints (referred to as Node 1—the distal endpoint, and Node 2—the proximal endpoint) along the direction of the tendinous fibers. The ROI was defined as the tissue bounded by a rectangular area that extended between the endpoints (Fig. 2). The ROI width was set to 0.75 mm for all trials and subjects, which was sufficient to ensure that only tendinous tissue was within the ROI for the subjects with the narrowest tendons. The endpoints of each ROI were chosen from the initial frame of each trial, such that the ROI extended as long as a length of the tendon ( $\sim$ 30 mm) while allowing for nodal displacements to remain within the image window during the twitch.

2) *Nodal Displacements:* Pixel displacements between successive frames were computed using correlation-based speckle tracking [16]. Two-dimensional normalized, cross-correlation functions,  $\rho_{nm}(k,l)$ , were first computed for each of the pixels within the ROI, by cross-correlating a kernel (2K+1 pixels axially by 2L+1 pixels laterally) centered about the pixel in the initial frame with a search region centered at the same pixel in the subsequent frame (1) (see above). In (1),  $F_1$  and  $F_2$  refer to the RF data in the first and second frames, while  $k$  and  $l$  refer to the displacements in the axial and lateral directions. A fixed kernel size of 15 pixels (0.3 mm long,  $K = 7$ ) by 3 pixels (0.5 mm wide,  $L = 1$ ) was used. The size of the search region was defined to allow maximum frame-to-frame displacements of 15 pixels (0.3 mm) and 6 pixels (1.0 mm) in axial and lateral directions, respectively.

After computing the correlation functions at each pixel, the correlation functions were spatially filtered along the length of the ROI to improve the signal-to-noise ratio [16]. To do this, the ROI was split into evenly spaced subintervals. The number of subintervals,  $M$ , was set to 100. The average normalized position of all pixels within each subinterval along the length of the ROI was first determined as

$$\bar{s}_j = \frac{\sum \bar{s}_{mn}}{N_j}, \quad \frac{j-1}{M} < \bar{s}_{mn} < \frac{j}{M}, \quad (2)$$

where  $N_j$  was the number of pixels in the  $j$ th subinterval,  $L$  was the current length of the ROI, and  $\bar{s}_{mn}$  was the normalized distance along the length of the midline of the ROI from the distal endpoint to the pixel. The correlation functions were then averaged over all pixels within each subinterval:

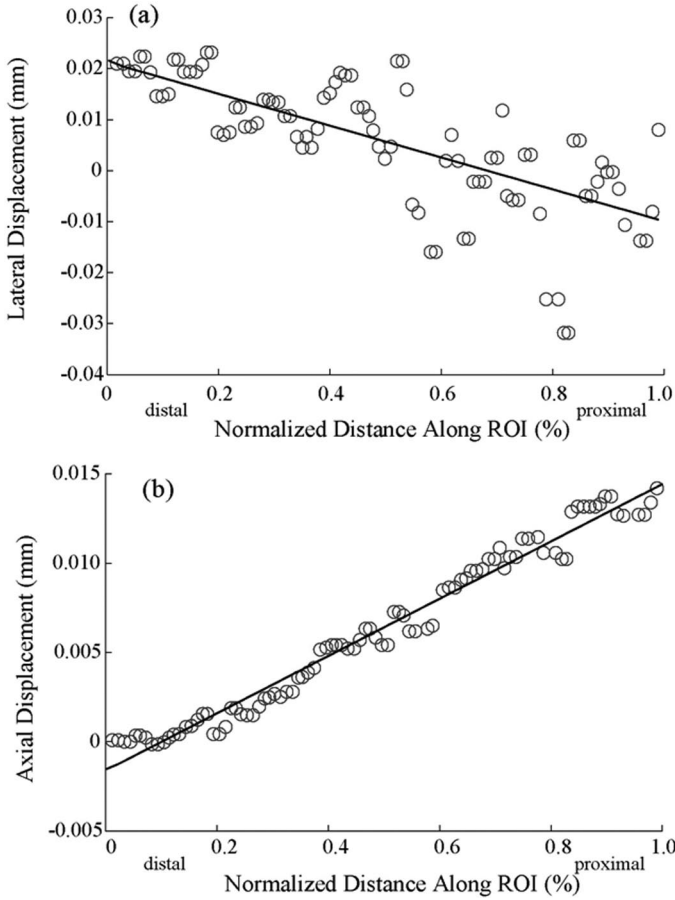


Fig. 3. A linear, least-squares fit of the lateral (a) and axial (b) sub-interval displacements was used to compute the nodal displacements between successive frames. For the example data shown, the coefficient of determination ( $R^2$ ) was 0.44 for the lateral displacements and 0.99 for the axial displacements.

$$\rho_j(k, l) = \frac{\sum \rho_{mn}(k, l)}{N_j}, \quad \frac{j-1}{M} < \bar{s}_{mn} < \frac{j}{M}, \quad (3)$$

resulting in a correlation function matrix  $\rho_j(k, l)$  for each subinterval along the ROI.

Nominal displacements of each subinterval were first estimated as the distance to the peak correlation coefficient in its corresponding correlation function matrix from the matrix center pixel. Subpixel displacements were then estimated by fitting a 2-D quadratic function to the  $3 \times 3$  pixel region of the correlation function matrix centered at the peak correlation coefficient and analytically determining the peak of this function [11]. This process resulted in estimates of the axial,  $u_j$ , and lateral,  $v_j$ , incremental displacements for each subinterval  $j$ .

Finally, the frame-to-frame displacements of the endpoint nodes in the axial ( $U_1$ ,  $U_2$ ) and lateral ( $V_1$ ,  $V_2$ ) directions were obtained by using a weighted linear least squares fit to best predict the subinterval displacements, assuming a linear strain model (Fig. 3)

$$\begin{Bmatrix} u_1 \\ u_2 \\ \vdots \\ u_M \end{Bmatrix} = \begin{bmatrix} (1 - \bar{s}_1) & \bar{s}_1 \\ (1 - \bar{s}_2) & \bar{s}_2 \\ \vdots & \vdots \\ (1 - \bar{s}_M) & \bar{s}_M \end{bmatrix} \begin{Bmatrix} U_1 \\ U_2 \end{Bmatrix} \quad (4)$$

$$\begin{Bmatrix} v_1 \\ v_2 \\ \vdots \\ v_M \end{Bmatrix} = \begin{bmatrix} (1 - \bar{s}_1) & \bar{s}_1 \\ (1 - \bar{s}_2) & \bar{s}_2 \\ \vdots & \vdots \\ (1 - \bar{s}_M) & \bar{s}_M \end{bmatrix} \begin{Bmatrix} V_1 \\ V_2 \end{Bmatrix}. \quad (5)$$

The peak correlations associated with each of the sub-interval displacement estimates were used as a weight parameter when solving this overdetermined set of equations (4) and (5) for the node displacements. Displacements associated with correlation coefficients below a desired threshold ( $= 0.70$ ) were excluded from the least squares calculations.

3) *Tendon Strain*: Node displacements were summed across successive frames to determine the cumulative motion of the ROI endpoints, which allowed for the ROI to translate, rotate, and change length over time. The twitch-induced cumulative engineering strain,  $\Delta\varepsilon$ , along the ROI was then computed from length  $L$  of the ROI in each frame:

$$\Delta\varepsilon = \frac{L - L_0}{L_0}, \quad (6)$$

where  $L_0$  was the initial length of the ROI before the twitch contraction stimulus. The performance of the elastographic tracking algorithm was first verified by analyzing synthetically generated RF data using a finite element model of soft tissue undergoing uniform deformation (see appendix). Accurate estimates of the frame-to-frame and cumulative strain were obtained when using the same lateral upsampling factor that was applied to the experimentally obtained images.

### C. Visual Analysis of Tendon Strain

The peak tendon strain was also estimated via visual inspection of the B-mode images similar to previous investigations [1], [3], [6]. The musculotendon junction (MTJ) was first located in an image acquired with the muscle in the pre-twitch state, and in the frame at peak displacement of the musculotendon junction during the induced twitch. The MTJ was defined to be the intersection of the upper (anterior) boundary of the tendinous tissues, including the aponeurosis and tendon, with the TA muscle and the upper (anterior) border of the TA muscle itself. This was determined by drawing straight intersecting lines along these muscle bounds (Fig. 2). From MTJ displacements, average tendon strain was then estimated as the net displacement of the MTJ normalized to the length of tendon from the MTJ to its insertion point at the medial

cuneiform and first metatarsal of the foot, which was previously measured experimentally.

#### D. Biomechanical Analyses

Load cell data were first used to estimate the net moment,  $M_A$ , about the ankle joint in the sagittal plane. It was assumed that all measured force was the result of TA muscle contractions about the ankle, resulting in an expression for the tendon force  $F^T$ :

$$F^T = \frac{M_A}{r_A^T} \quad (7)$$

where  $r_A^T$  is the tibialis anterior moment arm about the ankle (assumed to be 0.035 m [17]). The tendon engineering stress  $\sigma^T$  was then estimated by dividing the tendon force by the average cross-sectional area of the unloaded tendon,  $A_T$ , over the imaging region:

$$\sigma = \frac{F^T}{A^T}. \quad (8)$$

Tendon cross-sectional area was measured in ultrasound images at the distal end of MTJ view window when the tendon was unloaded. The calculated tendon stress was divided into the sum of the preload and incremental components,  $\sigma = \sigma_p + \Delta\sigma$ , where  $\sigma_p$  is the tendon preload stress, and  $\Delta\sigma$  is the change in tendon stress due to the induced twitch contractions.

For each trial, the tangential modulus of the tendon,  $E_{\text{tan}}$ , was calculated at the peak change in stress,  $\Delta\sigma_{\text{max}}$ , normalized by the peak cumulative strain,  $\Delta\varepsilon_{\text{max}}$ , during the twitch:

$$E_{\text{tan}} = \frac{\Delta\sigma_{\text{max}}}{\Delta\varepsilon_{\text{max}}}. \quad (9)$$

Cumulative strain, stress, and tangential moduli were calculated for each trial using both elastography and visual analyses. Peak values were then averaged across the 3 repeated trials for each of the preload conditions.

### III. RESULTS

The proposed algorithm was able to track tissue motion with reasonably high correlations for all twitch contractions with the exception of the zero preload condition (Table I). Over 82% of the subintervals had peak correlations that exceeded the 0.70 threshold correlation when a preload was present. However, the correlations were substantially reduced in the no-preload case, with only 18 to 71% of the sub-intervals having correlations that exceeded the 0.70 threshold. As a result for the remainder of this paper, we will only present strain estimates for the preload conditions.

The change in cumulative tendon strain following the stimulus exhibited characteristic twitchlike responses, involving a rapid increase in strain followed by a slower relaxation, as shown in Fig. 4(a). For all subjects and conditions, motion of the more proximal node preceded and was larger than the motion of the distal node, as shown in Fig. 4(b).

The elastography-based cumulative strains for each preload condition ranged from 0.06 to 0.80%. In a paired t-test, these values were significantly ( $p < 0.05$ ) larger than those obtained using visual inspection of the B-mode images, as shown in Fig. 5(a), where the cumulative change in strain ranged from 0.08% to 0.47%. The estimated preload tendon stress ranged from 4 to 35 MPa across the conditions tested. The resulting tangential elastic moduli were independent of the preload magnitude, averaging  $192 \pm 58$  MPa across all trials, as shown in Fig. 5(b).

At low preloads, twitch contraction times determined using elastography were significantly shorter than those estimated from either the visual strain or external force measures (Fig. 6). An average of 50 ms was required for the tendon to reach peak local strain at low preloads, with this value increasing to an average of 80 ms at the higher preloads.

### IV. DISCUSSION

This paper introduces the use of elastography-based analysis of RF data to characterize in vivo tendon strain during muscle twitch contractions. The approach was shown to provide reasonable estimates of the time-varying

TABLE I. PERCENTAGE OF SUBINTERVALS (OUT OF 100) THAT EXCEEDED THE CORRELATION THRESHOLD OF 0.70 WHEN TRACKING FRAME-TO-FRAME DISPLACEMENT FOR EACH OF THE PRELOAD CONDITIONS. SUBSTANTIALLY HIGHER CORRELATIONS WERE ACHIEVED WHEN THE TENDON WAS PRELOADED.

Preload (%MVC)	Subject				
	1	2	3	4	5
0%	65	32	42	19	71
10%	95	82	82	92	99
20%	96	94	80	95	99
30%	96	99	87	93	98
40%	97	99	85	95	100
50%	98	100	92	96	100

tendon strain and tangential modulus, provided that the tendon was initially preloaded.

The results obtained using elastographic imaging differ from those obtained using more traditional visual-based approaches. Visual approaches require the manual identification of anatomical landmarks (e.g., the musculotendon junction) from B-mode images. However, because only a single anatomical landmark at the MTJ can usually be identified, researchers typically assume the other end of the tendon is either held stationary or has moved in a way that can be ascertained in an unloaded calibration trial [1], [2], [6], [18]–[20]. Therefore, visual-based approaches can only provide an estimate of the average strain over a long segment of tendon. In contrast, an elastography-based approach is able to ascertain tendon strain using displacement measurements within the viewing window. This has the advantage of providing a more localized estimate of the strain. In this study, we have shown that the peak local strain computed using elastography occurred earlier and was typically larger than the visual-based estimate of average strain over the entire tendon. Our estimates of twitch contraction time based on the local strain measures were significantly faster at low preloads than literature values that are based on external force measures [21]. This difference may reflect the musculotendon dynamic processes in which the contraction process originates at the muscle belly and propagates to the end. As a result, tendon tissue nearer to the muscle belly is likely to be stretched earlier than more distal tissue, as was typically observed in the relative motion of the 2 endpoints of the ROI (Fig. 4).

A prior study used correlation-based analysis of B-mode images to track small amplitude muscle stretch of the plantar flexors during quiet stance [15], [22]. However, the use of B-mode images requires the use of fairly large kernel sizes (e.g., 5 mm square in [15]) to track motion. In contrast, we were able to obtain displacement estimates with much smaller kernels ( $0.5 \times 0.3$  mm) using the RF data. This distinction is achieved by using the phase information in the raw RF data, which has been shown to facilitate accurate tracking and the resolution of spatial variations in axial strain [10]. Although our current method does not provide spatial resolution (it provides only one strain value along the laterally oriented tendon), our long-term goal is to track multiple nodal points along the ROI so as to characterize spatial variations in tendon strain. Our approach can also potentially be applied to track muscle strains by defining the ROI along the fibers of the muscle rather than the tendon.

The coupling of cumulative strain estimates with biomechanical force data allowed for an estimate of the tangential elastic modulus of the tibialis anterior tendon. Prior studies have shown that tendon exhibits less stiffness in a low-load toe region, but then maintains a constant magnitude as load increases and all the tendinous fibers become taut [23]. We were not able to estimate the modulus for the zero-load case and thus were unable to fully capture the toe-region. However at low-to-moderate loads (10–50%

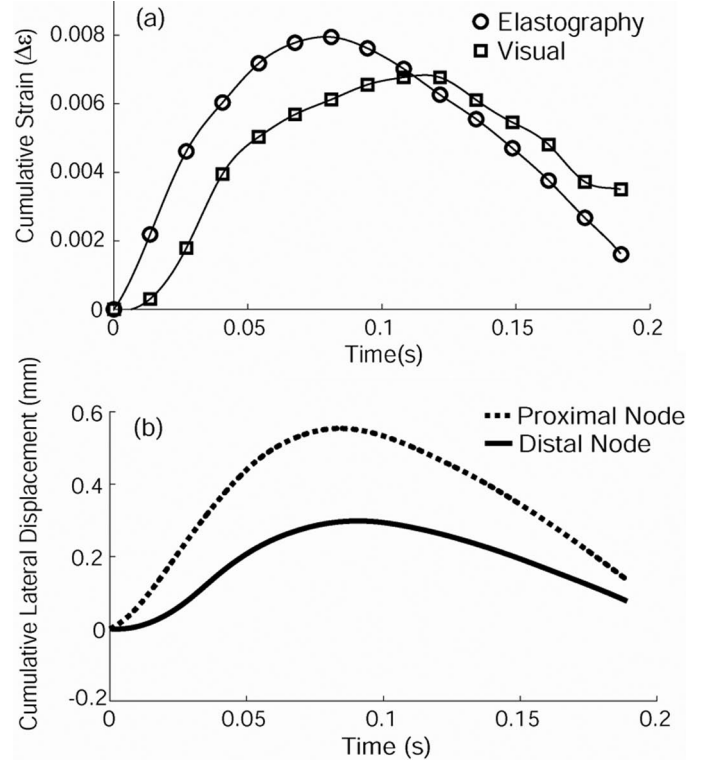


Fig. 4. (a) The strain computed from the elastographic analysis of RF data peaks earlier and has a larger magnitude than that determined using visual analysis of the B-mode images. (b) Lateral displacement of the proximal node on the ROI tended to precede motion of the more distal node. Twitch contraction time was defined as the time after the onset of movement at which peak change in strain occurred.

of maximum isometric force), the estimated modulus was found to be fairly constant averaging 192 MPa, which is in the lower range of stiffnesses (157 to 530 MPa) previously estimated for the TA tendon [6]. It is possible that higher preloads may have resulted in greater tangential stiffness.

Our approach was not well suited for tracking the TA tendon motion when the stimulation pulse was applied to a relaxed muscle (Table I). This limitation could potentially result from the microstructure of the tendons, in which the fibers are initially slack before being loaded [23]. As a result, some out-of-plane motion may occur as the fibers become taut, which may have degraded the cross-correlation functions, which inherently assume planar motion. It is possible that further increasing the frame rate may reduce the decorrelation that occurs due to out-of-plane and lateral motion, and hence improve the incremental displacement estimates under slack tendon conditions.

The primary challenge with using elastographic approaches for characterizing musculotendon mechanics is that most of the motion is perpendicular to the beam direction. Such lateral motion tracking tends to be an order of magnitude less accurate than axial displacement estimates using current approaches [11]. Further study is needed to ascertain whether alternative lateral tracking schemes [12] or beam steering [24] may be able to improve the accuracy of lateral displacement estimates, which would further the long-term goal of estimating spa-

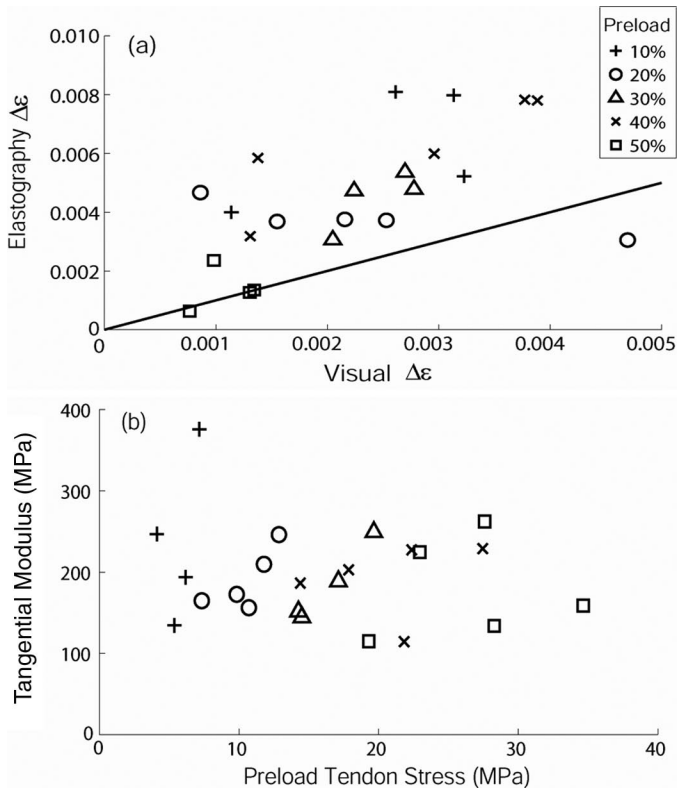


Fig. 5. (a) Peak tendon strains measured using elastography were significantly larger than peak strains estimated using visual inspection of B-mode images. The trend line shown represents a 1:1 ratio. (b) The tangential moduli of the tendon, ratios of change in stress to change in strain, were relatively constant across the range of preload conditions considered.

tial variations in strain throughout a 2-D image region. In addition, this study only addressed the tracking of tendon motion during short duration twitch contractions involving less than 1% cumulative strain. The relatively short interval and small motion was advantageous when summing frame-to-frame motion, because errors can accumulate over longer duration trials.

The accuracy of cumulative displacements is particularly affected by bias errors, which can result from interpolation of the correlation function [25], [26]. Analysis of the synthetic data by our tracking algorithm suggests that upsampling the data in the lateral direction was important for reducing bias effects (Fig. A1 in the appendix). Finally, strain was computed over a region of interest that included both free tendon and aponeurosis (i.e., tendinous tissue within the muscle belly). This was done so that the MTJ would be visible in all trials, providing us with a visual comparison. However, it remains unclear whether the aponeurosis undergoes similar [18], [20] or greater strain [1], [2] than the free tendon. The elastography approach could potentially address this issue provided that the experiments are repeated with the transducer located both proximally and distally to the MTJ.

In summary, we have demonstrated the use of elastography for estimating the time evolution of tendon strain during twitch contractions. This approach can provide lo-

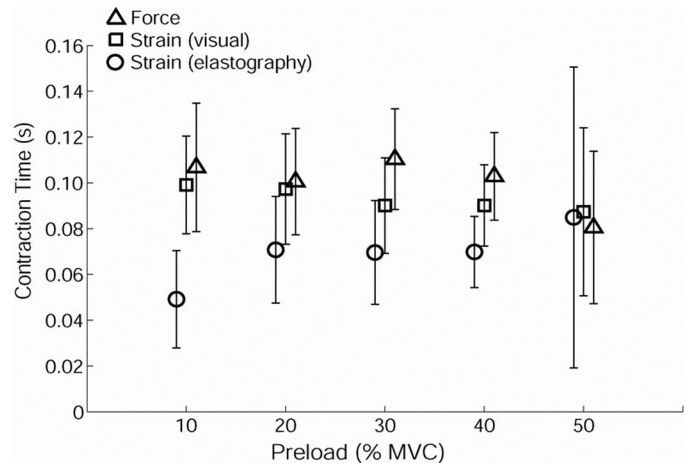


Fig. 6. Average ( $\pm$  sd) time to peak force and peak cumulative strain as assessed using both visual and elastographic approaches. Note that peak local strains (elastography) occurred much earlier than the average strain over the tendon when the muscle had low preloads.

cal estimates of tendon strain for a short region of interest and, when coupled with biomechanical data, tangential tendon stiffness. Such analyses were shown to provide unique insights into musculotendon dynamics and may find additional clinical application in distinguishing the changes in tendon properties associated with pathologies.

## APPENDIX

We used synthetic data to investigate the performance of the local strain estimation algorithm described in the methods. Our purpose was to assess the accuracy of the algorithm and to evaluate the effect of lateral interpolation of RF data on lateral strain estimates. A uniformly elastic numerical tissue mimicking (TM) phantom was constructed with a thickness of 10 mm, width of 40 mm, and depth of 40 mm using finite element analysis (FEA) software (ANSYS Inc., Canonsburg, PA). The Young's modulus was set to 10 kPa, and the material was assumed to be nearly incompressible, with a Poisson's ratio of 0.495. The bottom boundary of the tissue was constrained from moving axially. Zero friction was assumed at the bottom interface, allowing for lateral slip motion to occur. Uniform pressure was applied along the top of the tissue such that the material underwent successive normal strains of 0.5% for 10 successive steps. Thus, we produced a series of 11 images in which the lateral strain was zero in the first frame and uniformly incremented up by 0.245% in each successive frame to a final cumulative lateral strain of 2.45%.

The axial and lateral displacement information was then used in an ultrasound simulation program [27] to generate pre and post-compression RF echo signal data at the end of each compression step. The simulation program calculates the frequency domain response of ultrasound waves propagating through a scattering medium comprised of 100  $\mu\text{m}$  radius polystyrene beads, which were random-

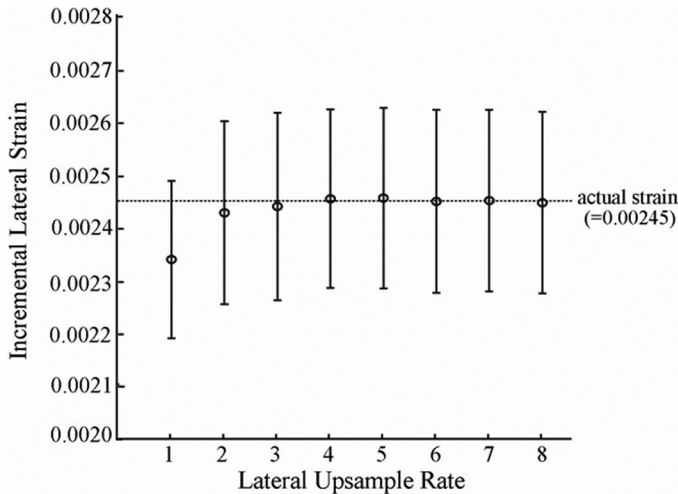


Fig. A1. The mean ( $\pm 1$  sd) incremental (frame-to-frame) strain estimates along a 30 mm ROI that was initially aligned horizontally in the image plane. Lateral upsampling of the data was important to achieve unbiased estimates of the actual strain.

ly distributed in the phantom at a high enough number density to ensure Rayleigh scattering [28]. The frequency responses were transformed back to the time domain to obtain ultrasound radiofrequency frames. Ultrasound echo signals obtained from a linear array transducer was modeled, which consisted of  $0.1 \times 10 \text{ mm}^2$  elements with a 0.15 mm center-to-center element separation, with the transmit beam formed using 128 consecutive elements for the aperture. The incident pulses were modeled as Gaussian shaped with an 8 MHz center frequency and a 100% bandwidth and sampled at 52 MHz. RF data were generated assuming a constant sound speed of 1540 m/s and attenuation was not included.

We compared the performance of our strain estimation algorithm for a 30 mm long ROI that was initially centered at a depth of 10 mm in the imaging plan. We analyzed 2 cases: when the ROI was initially horizontal, and when the ROI was oriented at a  $10^\circ$  angle in the imaging plane, which represented the average tendon orientation observed in our imaging study (Fig. 2). For each condition, we used linear interpolation ratios ranging from a factor of 1 to 8.

Our results show that upsampling of the data in the lateral direction is critical to achieve unbiased estimates of lateral strain (Fig. A1). Without upsampling, the frame-to-frame lateral strain estimates averaged 0.235% (s.d. = 0.015%), which was less than the actual lateral strain of 0.245%. Biasing likely arose due to inaccuracy in the quadratic interpolation method for estimating the correlation peak on the basis of the values to either side [25], [26]. Upsampling by a factor of 4 reduced these errors, resulting in average frame-to-frame lateral strain estimates of 0.246% (s.d. = 0.017%), which was close to the actual lateral strain value of 0.245%. We also assessed the accuracy of errors in tracking strains in an obliquely oriented ROI that had a  $10^\circ$  orientation relative to the horizontal, which was similar to the orientation of the TA tendon in

the experimental trials (Fig. 2). Strain errors again reduced when an up sampling rate of 4 was used, with average frame-to-frame strain estimates of 0.222% (s.d. = 0.012%) being just slightly lower than the actual strain of 0.227% along the obliquely oriented ROI. Based on this simulation analysis, we conclude that our tracking algorithm can provide reasonably accurate estimates of strain along a laterally oriented ROI, provided that upsampling is used to improve the lateral spatial density of the raw RF data.

We do note that our model did not account for the complex interaction of transversely isotropic fibers and tendons. Models that account for these musculotendon properties and unique architectures are an area of active research interest [29], and when more fully developed, could provide further insights into the use of elastographic techniques to measure in vivo tendon strains.

#### ACKNOWLEDGMENTS

We gratefully acknowledge the assistance of Mohammed Asadullah, Shyam Bharat, and Hao Chen in the data collections, and Min Rao for providing the synthetic data.

#### REFERENCES

- [1] C. N. Maganaris and J. P. Paul, "Load-elongation characteristics of in vivo human tendon and aponeurosis," *J. Exp. Biol.*, vol. 203, pt. 4, pp. 751–756, 2000.
- [2] C. N. Maganaris, "Tensile properties of in vivo human tendinous tissue," *J. Biomech.*, vol. 35, no. 8, pp. 1019–1027, 2002.
- [3] C. N. Maganaris and J. P. Paul, "In vivo human tendinous tissue stretch upon maximum muscle force generation," *J. Biomech.*, vol. 33, no. 11, pp. 1453–1459, 2000.
- [4] S. Kurokawa, T. Fukunaga, A. Nagano, and S. Fukashiro, "Interaction between fascicles and tendinous structures during counter movement jumping investigated in vivo," *J. Appl. Physiol.*, vol. 95, no. 6, pp. 2306–2314, 2003.
- [5] M. Ito, H. Akima, and T. Fukunaga, "In vivo moment arm determination using B-mode ultrasonography," *J. Biomech.*, vol. 33, no. 2, pp. 215–218, 2000.
- [6] M. Ito, Y. Kawakami, Y. Ichinose, S. Fukashiro, and T. Fukunaga, "Nonisometric behavior of fascicles during isometric contractions of a human muscle," *J. Appl. Physiol.*, vol. 85, no. 4, pp. 1230–1235, 1998.
- [7] S. F. Levinson, M. Shinagawa, and T. Sato, "Sonoelastic determination of human skeletal muscle elasticity," *J. Biomech.*, vol. 28, no. 10, pp. 1145–1154, 1995.
- [8] T. Fukunaga, Y. Kawakami, K. Kubo, and H. Kanehisa, "Muscle and tendon interaction during human movements," *Exerc. Sport Sci. Rev.*, vol. 30, no. 3, pp. 106–110, 2002.
- [9] M. Ishikawa, P. V. Komi, M. J. Grey, V. Lepola, and G. P. Brüggemann, "Muscle-tendon interaction and elastic energy usage in human walking," *J. Appl. Physiol.*, vol. 99, no. 2, pp. 603–608, 2005.
- [10] J. Ophir, S. K. Alam, B. Garra, F. Kallel, E. Konofagou, T. Krouskop, and T. Varghese, "Elastography: Ultrasonic estimation and imaging of the elastic properties of tissues," *Proc. Inst. Mech. Eng. [H]*, vol. 213, no. 3, pp. 203–233, 1999.
- [11] E. S. Ebbini, "Phase-coupled two-dimensional speckle tracking algorithm," *IEEE Trans. Ultrason. Ferroelectr. Freq. Control*, vol. 53, no. 5, pp. 972–990, 2006.
- [12] X. Chen, M. J. Zohdy, S. Y. Emelianov, and M. O'Donnell, "Lateral speckle tracking using synthetic lateral phase," *IEEE Trans. Ultrason. Ferroelectr. Freq. Control*, vol. 51, no. 5, pp. 540–550, 2004.
- [13] K. Kaluzynski, X. Chen, S. Y. Emelianov, A. R. Skovoroda, and M. O'Donnell, "Strain rate imaging using two-dimensional speckle

- tracking," *IEEE Trans. Ultrason. Ferroelectr. Freq. Control*, vol. 48, no. 4, pp. 1111–1123, 2001.
- [14] R. S. Witte, K. Kim, B. J. Martin, M. O'Donnell, "Effect of fatigue on muscle elasticity in the human forearm using ultrasound strain imaging," in *Proc. 28th Annu. Int. Conf. IEEE Engineering in Medicine and Biology Society*. New York, 2006, pp. 4490–4493.
- [15] I. D. Loram, C. N. Maganaris, and M. Lakie, "Use of ultrasound to make noninvasive in vivo measurement of continuous changes in human muscle contractile length," *J. Appl. Physiol.*, vol. 100, no. 4, pp. 1311–1323, 2006.
- [16] M. A. Lubinski, S. Y. Emelianov, and M. O'Donnell, "Speckle tracking methods for ultrasonic elasticity imaging using short-time correlation," *IEEE Trans. Ultrason. Ferroelectr. Freq. Control*, vol. 46, no. 1, pp. 82–96, 1999.
- [17] C. N. Maganaris and J. P. Paul, "In vivo human tendon mechanical properties," *J. Physiol.*, vol. 521, no. Pt 1, pp. 307–313, 1999.
- [18] L. Mademli, A. Arampatzis, and M. Walsh, "Effect of muscle fatigue on the compliance of the gastrocnemius medialis tendon and aponeurosis," *J. Biomech.*, vol. 39, no. 3, pp. 426–434, 2006.
- [19] K. Kubo, H. Kanehisa, and T. Fukunaga, "Effects of viscoelastic properties of tendon structures on stretch—shortening cycle exercise in vivo," *J. Sports Sci.*, vol. 23, no. 8, pp. 851–860, 2005.
- [20] A. Arampatzis, S. Stafilidis, G. DeMonte, K. Karamanidis, G. Morrey-Klapsing, and G. P. Brüggemann, "Strain and elongation of the human gastrocnemius tendon and aponeurosis during maximal plantarflexion effort," *J. Biomech.*, vol. 38, no. 4, pp. 833–841, 2005.
- [21] D. M. Connelly, C. L. Rice, M. R. Roos, and A. A. Vandervoort, "Motor unit firing rates and contractile properties in tibialis anterior of young and old men," *J. Appl. Physiol.*, vol. 87, no. 2, pp. 843–852, 1999.
- [22] I. D. Loram, C. N. Maganaris, and M. Lakie, "Paradoxical muscle movement in human standing," *J. Physiol.*, vol. 556, no. Pt 3, pp. 683–689, 2004.
- [23] U. Proske and D. L. Morgan, "Tendon stiffness: Methods of measurement and significance for the control of movement. A review," *J. Biomech.*, vol. 20, no. 1, pp. 75–82, 1987.
- [24] M. Rao, Q. Chen, H. Shi, T. Varghese, E. L. Madsen, J. A. Zagzebski, and T. A. Wilson, "Normal and shear strain estimation using beam steering on linear-array transducers," *Ultrasound Med. Biol.*, vol. 33, no. 1, pp. 57–66, 2007.
- [25] I. Céspedes, Y. Huang, J. Ophir, and S. Spratt, "Methods for estimation of subsample time delays of digitized echo signals," *Ultrason. Imaging*, vol. 17, no. 2, pp. 142–171, 1995.
- [26] R. J. Housden, A. H. Gee, G. M. Treece, and R. W. Prager, "Subsample interpolation strategies for sensorless freehand 3D ultrasound," *Ultrasound Med. Biol.*, vol. 32, no. 12, pp. 1897–1904, 2006.
- [27] Y. D. Li and J. A. Zagzebski, "A frequency domain model for generating B-mode images with array transducers," *IEEE Trans. Ultrason. Ferroelectr. Freq. Control*, vol. 46, no. 3, pp. 690–699, 1999.
- [28] R. F. Wagner, S. W. Smith, J. M. Sandrik, and H. Lopez, "Statistics of speckle in ultrasound B-scans," *IEEE Trans. Sonics Ultrason.*, vol. 30, no. 3, pp. 156–163, 1983.
- [29] S. S. Blemker and S. L. Delp, "Three-dimensional representation of complex muscle architectures and geometries," *Ann. Biomed. Eng.*, vol. 33, no. 5, pp. 661–673, 2005.

**Joe Farron, Tomy Varghese, and Darryl G. Thelen** biographies and pictures not available at time of publication.